HHS Public Access

Author manuscript

Anal Chem. Author manuscript; available in PMC 2017 August 14.

Electrophoretic Separation of Single Particles Using Nanoscale Thermoplastic Columns

Kumuditha M. Weerakoon-Ratnayake[†,‡], **Franklin I. Uba**[§], **Nyoté J. Oliver-Calixte**[†,‡], and **Steven A. Soper**[*,†,‡,§,∥,⊥]

[†]Department of Chemistry, Louisiana State University, Baton Rouge, Lousiana 70803, United States

[‡]Department of Biomedical Engineering, University of North Carolina at Chapel Hill, Chapel Hill, North Carolina 27599, United States

[§]Department of Chemistry, University of North Carolina at Chapel Hill, Chapel Hill, North Carolina 27599, United States

[∥]Center of Biomodular Multiscale Systems for Precision Medicine, University of North Carolina at Chapel Hill, Chapel Hill, North Carolina 27599, United States

[⊥]Ulsan National Institute of Science and Technology, Ulsan 44919, South Korea

Abstract

Phenomena associated with microscale electrophoresis separations cannot, in many cases, be applied to the nanoscale. Thus, understanding the electrophoretic characteristics associated with the nanoscale will help formulate relevant strategies that can optimize the performance of separations carried out on columns with at least one dimension below 150 nm. Electric double layer (EDL) overlap, diffusion, and adsorption/desorption properties and/or dielectrophoretic effects giving rise to stick/slip motion are some of the processes that can play a role in determining the Efficiency of nanoscale electrophoretic separations. We investigated the performance characteristics of electrophoretic separations carried out in nanoslits fabricated in poly(methyl methacrylate), PMMA, devices. Silver nanoparticles (AgNPs) were used as the model system with tracking of their transport via dark field microscopy and localized surface plasmon resonance. AgNPs capped with citrate groups and the negatively charged PMMA walls (induced by O_2 plasma modification of the nanoslit walls) enabled separations that were not apparent when these particles were electrophoresed in microscale columns. The separation of AgNPs based on their size without the need for buffer additives using PMMA nanoslit devices is demonstrated herein.

Operational parameters such as the electric field strength, nanoslit dimensions, and buffer composition were evaluated as to their effects on the electrophoretic performance, both in terms of Efficiency (plate numbers) and resolution. Electrophoretic separations performed at high electric field strengths (>200 V/cm) resulted in higher plate numbers compared to lower fields due to the absence of stick/slip motion at the higher electric field strengths. Indeed, 60 nm AgNPs could be separated from 100 nm particles in free solution using nanoscale electrophoresis with 100 μm long columns.

Graphical abstract
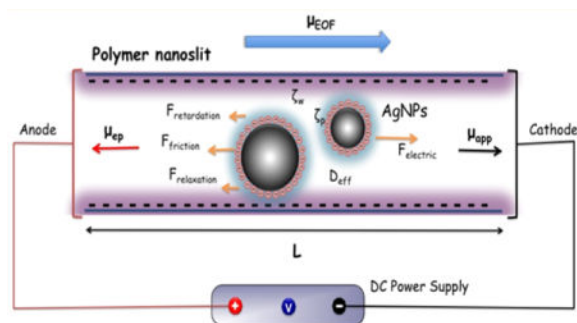
Over the past decade, microchip capillary electrophoresis (microchip-CE) has gained relevance because of its unique operating characteristics, such as the ability to assay hundreds of samples simultaneously, low sample and reagent consumption, and the ease of integrating multiple sample processing steps into a single platform.[1–7] However, the electrophoretic separation process in microchip-CE is fundamentally similar to capillary-based CE; the separation resolution depends primarily on differences in the electrophoretic mobility of the targets and reducing zonal dispersion, which is primarily determined by longitudinal diffusion in well-designed systems. In some cases, the lack of separation in free solution is circumvented by using buffer additives. For instance, because of the free draining behavior of single and double-stranded DNA molecules in free solution, electrophoretic separations require the incorporation of a 3D porous gel. Alternative additives are surfactants used above their critical micelle concentration to form pseudostationary phases.

Nanofluidics, which utilizes structures with one (nanoslits) or two (nanochannels) critical dimensions <150 nm, have provided platforms for unique electrophoretic phenomena that are not available in microscale environments.[8,9] Nanochannels and/or nanoslits have been applied in many different analytical separations,[10,11] manipulation and detection of single molecules,[12] and control of molecular transport.[13,14] Nanofluidics has also been used for electrophoresis as well. For example, it has been shown that dsDNA fragments can be separated in glass-based nanoslits without the need for a sieving gel when the channel dimensions are on the order of the Debye length (λ_D).[15]

There have been a few studies discussing the theoretical basis of nanoscale electrophoresis.[16–18] The challenge here is that existing theories applicable to microscale systems do not necessarily describe fundamental nanoscale phenomena. Theories and experimental studies relevant to nanoscale electrokinetic separations have appeared in

several reports.[19,20] For example, ion transport with d/λ_D (d = channel critical dimension) ratios ranging from 1 to 10 show anomalous transport behavior, such as charge-dependent ion mobilities due to transverse electromigration (TEM) resulting from solute/wall electrostatic effects.[15,21–23] Pennathur and Santiago showed that electrokinetic separations in nanoslits were dependent on ion valence, ζ (zeta potential), ion mobility, and λ_D.[15,21] Garcia et al.[24] reported the electrokinetic separation of Alexa 488 (negatively charged) and rhodamine B (neutral) fluorescent dyes in glass-based nanochannels with widths between 35 and 200 nm. The mobility of the fluorescent dyes varied with their inherent charge and the extent of wall interactions.

Glass and quartz have been widely used as substrates for micro- and nanofluidic devices because of their well-established surface chemistry, excellent optical properties, and well-developed fabrication technologies. All of the aforementioned nanoscale electrophoresis studies were performed in glass-type devices. These materials ensure an electrical insulating interface and provide relatively large amounts of surface charge when in contact with aqueous solutions generating a large electroosmotic flow (EOF).[25]

Recently, thermoplastics have generated interest as nanofluidic devices because of their biocompatibility, optical properties comparable to glass substrates in some cases and their ability to be manufactured in a high production mode at low-cost using nanoreplication modalities, such as nanoimprint lithography (NIL). NIL has proven to be successful in patterning structures to sub-10 nm scales,[26–29] with the ultimate resolution seemingly determined by the minimum feature size associated with the imprinting tool.[30] Several researchers have reported the fabrication of nanofluidic devices in thermoplastics.[31–33] We recently reported a low-cost, high throughput scheme for the production of nanochannels and nanoslits in thermoplastics.[34,35]

Previous work has shown the ability to separate submicrometer-sized particles based on their unique electrophoretic mobility.[36] Liu et al.[37] were able to separate silver nanoparticles (AgNPs) in the presence of an SDS surfactant using CE; no separation was achievable using free solution electrophoresis. While there have been reports on the separation of spherical nanoparticles using conventional or microchip CE, only a few studies have reported the electrophoretic transport behavior of noble metal nanoparticles in nanofluidic domains;[17,18,38] these studies used glass-based devices, however.

Herein, we report the separation of single AgNPs in thermoplastic nanoslit devices. AgNPs were used in this study because the localized surface plasmon resonance (LSPR) of these particles coupled with dark-field microscopy could be used to track their transport properties free from photobleaching.[7] In this manuscript, we discuss the effects of polymer-based nanoslit depth (150 and 400 nm), salt concentration, and field strength on the electrophoretic properties of 60 and 100 nm diameter AgNPs.

EXPERIMENTAL METHODS

Materials

Silicon ⟨100⟩ (Si) wafers were purchased from University Wafers (Boston, MA). Poly(methyl methacrylate), PMMA, substrates and cover plates were purchased from Good Fellow (Berwyn, PA) and cyclic olefin copolymer (COC 6017) was purchased from TOPAS Advanced Polymers (Florence, KY). The antiadhesion coating material, (tridecafluoro-1,1,2,2-tetrahydrooctyl) tricholorosilane (T-silane), was purchased from Gelest, Inc. (Morrisville, PA). Citrate capped AgNPs (60 and 100 nm in diameter) were purchased from Nanocomposix, Inc. (San Diego, CA) and suspended in an aqueous 2 mM citrate buffer (Fisher Scientific, Philadelphia, PA). The concentrations of the AgNP solutions were adjusted so that single particle events could be tracked within the PMMA nanoslits. All dilutions were performed using 18 MΩ/cm Milli-Q water (Millipore) with citrate buffer (pH = 7.0). The final concentrations were ~10^8 particles/μL. All solutions were filtered through 0.2 μm membranes (Thermo Scientific Nalgene syringe filters) prior to use. Particle size variation was reported by the manufactures to be ~10% (CV).

Fabrication of Nanofluidic Devices

The nanofluidic devices were fabricated using procedures we have reported.[32,34,35,39] Specific information on the fabrication process can be found in the Supporting Information. The metrology of the Si master, the resin stamp, and the replicated PMMA nanofluidic device can be found in Figure S1 (see the Supporting Information).

Dark-Field Microscopy Imaging

Dark-field microscopy was used to track single AgNPs electrophoretically moving through nanoslits under an applied electric field. Noble metal nanoparticles such as Ag, Au, and Cu have unique surface plasmon resonances that depend on their size, shape, and dielectric constant of the surrounding medium.[40,41] The AgNPs used herein have high yields for LSPR scattering. Compared to a single fluorescent molecule such as R6G, a 2 nm AgNP has a 10^4-fold higher photon yield making them easily tracked for long periods of times without photobleaching issues (Figure S2).[40–42]

A schematic of the imaging system is shown in Figure 1A. It consisted of an inverted microscope (Leica DMIRB) operated in a dark-field imaging mode, a COOLSNAP B/W EMCCD (Photometric), an excitation condenser with a high numerical aperture (NA = 0.9), and a 100× oil immersion objective with an adjustable numerical aperture (NA = 1.4–0.6). A 100 W halogen lamp was used as the excitation source. The filtered excitation light was incident onto the PMMA nanofluidic device and the scattered light from the AgNPs was transmitted through the objective and focused onto an EMCCD camera. All events were acquired at 3 ms exposure times with a 650 × 50 pixel region of interest that spans the entire length and width of a single nanoslit. A custom designed image-J macro was used to sort signals from aggregates of AgNPs from that of the monodispersed nanoparticles. The measured electrophoretic migration times were used to compute electrophoretic parameters of the AgNPs such as their electrophoretic mobility.

Nanoscale Electrophoretic Separations

A PMMA nanofluidic device was mounted on a sample holder and placed on a leveled sample stage of the dark-field microscope. Two platinum electrodes were inserted into reservoirs and an electric potential was applied longitudinally across the nanoslit using a dc-power supply (see Figure 1B). The electric fields used in these experiments ranged between 100 V/cm and 1500 V/cm. Prior to the electrophoresis, the assembled nanofluidic device, which was made in PMMA, was initially primed with a 50% v/v methanol/water mixture followed by multiple water rinses prior to introduction of the running buffer. After the channels were completely filled with the running buffer, the AgNP solution prepared in citrate buffer was injected into an access microchannel poised on the nanofluidic device and electrophoresed using the appropriate field strength through the nanoslit.

RESULTS AND DISCUSSION

Single AgNP Tracking

A description of the devices used for the AgNP nanoscale electrophoresis experiments is provided in the Supporting Information as well as SEMs of some of these devices (Figure S1). A picture of a finished device can be seen in Figure 1B. In all cases, the nanofluidic devices consisted of a PMMA substrate containing the fluidic network and a PMMA cover plate. Figure S1 shows SEMs and profilometer traces of the nanoslits used as columns for the electrophoresis.

The probability of occupancy (P_0) of an entity within a volume element can be calculated from

$$P_o = D_v C \quad (1)$$

where C is the concentration of the targets (in this case, the number of AgNP per mL of solution) and D_v is the detection volume, which was defined as the nanoslit electrophoresis column (75 fL for a 150 nm deep nanoslit with a width of 5 μm and column length of 100 μm). The concentration of AgNPs was adjusted to keep only a single particle resident within the electrophoresis column at a time to aid in single particle tracking. If $P_o = 0.01$, the probability of double occupancy is 0.01% and thus, almost all events could be ascribed to single particle events. At $P_o = 0.01$ and $D_v = 75$ fL, the particle concentration required to meet this criteria was 1.3×10^8/mL. Therefore, the particle concentration used in our experiments was set at 10^8/mL; the probability of double occupancy was minimal.

In the absence of an electric field applied across the nanoslit, only Brownian motion of particles was observed. However, in the presence of an electric field, the AgNPs were electrophoretically transported through the nanoslits. We noted that the number of particles entering the nanoslits per unit time was found to increase with increases in the electric field. Wynne et al. observed similar behavior for negatively charged polystyrene beads electrophoresing through a glass nanofluidic device.[18] They hypothesized that for the case of negatively charged walls and negatively charged particles, as in our case, lower buffer concentrations should produce a thicker EDL resulting in particle exclusion from the

nanoslit. However, using the PMMA nanoslit devices and buffer concentrations employed herein, we did not observe exclusion effects when a certain voltage threshold was exceeded (see below) in spite of the fact that the channel walls and AgNPs carried negative charges.

Nanoscale Electrophoresis

Figure 1C shows the electrophoretic transport of a single AgNP in a nanoslit using an electric field strength of 200 V/cm and Figure 1D shows selected frames from a time-lapse image sequence for 60 nm AgNPs translocating through a PMMA nanoslit. The average time for the AgNPs to migrate through the nanoslit (length = 100 μm) was 1.3 s at this field strength. This corresponded to a linear velocity of 0.0077 cm/s or an apparent electrophoretic mobility of 3.8×10^{-5} cm^2/(V s). We also observed that both the 60 and 100 nm AgNPs migrated from anode to cathode, suggesting that the electroosmotic flow (EOF) induced by the nanoslit was greater than the electrophoretic mobility of the AgNPs; citric capped AgNPs. Citric acid is a tricarboxylic acid (pK_{a1} 3.13, pK_{a2} 4.77, pK_{a3} 6.4).[43] At pH 7.4, ~90.9% of the carboxyl groups of the citrate caps associated with the AgNPs are deprotonated imposing an overall negative charge to the AgNPs inducing an electrophoretic mobility of cathode to anode movement with an EOF moving from anode to cathode due to the negative surface charge of PMMA following O$_2$ plasma treatment.[34]

For an electrolyte, the Debye length, λ_D, can be calculated from

$$\lambda_D = \sqrt{\frac{\varepsilon_0 \varepsilon_r k_B T}{2 n_{bulk} z^2 e^2}} \quad (2)$$

where ε_0 is the permittivity of free space, ε_r represents the dielectric constant of the carrier electrolyte, k_B is the Boltzmann's constant, T is temperature of the electrolyte, n_{bulk} is the bulk ion concentration, z is the valency of the ions, and e is the charge of an electron.[44] λ_D can vary from a few Angstrom (Å) to a few hundred nanometers (nm). For a 2.0 mM citrate buffer, λ_D is ~6 nm while for 0.05 mM, λ_D is ~35 nm. At these buffer concentrations and considering a 150 nm slit (d), the ratio of the slit depth to λ_D (d/λ_D) is 25 for 2.0 mM citrate and 4.3 for the 0.05 mM citrate buffer. This indicates that predominately plug flow would be observed for the high concentration buffer and a more parabolic flow profile for the low buffer concentration in the 150 nm deep nanoslit. However, plug flow would be expected at both buffer concentrations for the 400 nm deep nanoslit.

Figure 2 shows histograms (100 events) of the electrophoretic migration times for the 60 nm (blue stripes) and 100 nm (red stripes) AgNPs transported electrokinetically through a 150 nm nanoslit in 0.05 mM citrate buffer using applied electric fields of 100, 200, 500, and 1500 V/cm. We observed "stick/slip" motion of the AgNPs at electric field strengths of 100 and 200 V/cm. This effect was previously observed for DNA translocation studies in nanocolumns[34,45,46] and arose from adsorption/desorption behavior of the solute with the channel walls.[47–49] In addition, this stick/slip motion can arise from dielectrophoretic trapping as well, which results from column wall surface roughness producing inhomogeneity in the electric field.[34]

When a negatively charged particle electrophoretically translocates through nanoscale columns with negatively charged walls under low buffer ionic strengths, it interacts both hydrodynamically and electrically with the channel walls.[34] Under low electric fields, Brownian motion dominates with the possibility of inducing potential wall interactions even when the solute (AgNPs) carries a net charge similar to the column walls, which in this case consisted of PMMA that had been O_2 plasma treated.[34] However, under high fields, electrokinetic forces become dominant and the particle travels predominately longitudinally through the column with minimal wall interactions (see Figure S3).

For O_2 plasma activated PMMA surfaces, the surface charge density has been reported to be -38.3 mC/m^2, yielding ζ of -57.1 mV, but these values are highly dependent on the dosing level of the plasma (time and power).[34] For O_2 plasma treated PMMA nanofluidic devices, there was a propensity for the negatively charged particles to not enter the nanoslits until a threshold (on-set) voltage was reached, which allowed the AgNPs to be continuously injected into the nanoslit. This onset voltage was found to be higher using low ionic strength buffers because of the thicker EDL compared to higher ionic strength buffers. For the 150 nm nanoslits, the on-set voltage was found to be ~10 V/cm in a 2.0 mM citrate buffer while in 0.05 mM buffer, this value increased to ~20 V/cm for the same nanoslit device. In all nanoscale electrophoresis experiments performed using PMMA devices, we did not observe concentration polarization effects at the nanoslit entrance. We also note that in all cases, the AgNPs traveled from anode to cathode irrespective of the nanoslit dimensions and carrier electrolyte composition, meaning that the EOF was greater than the electrophoretic mobility of both AgNP sizes.

The apparent mobility (μ_{app}) of the particles is the summation of their electrophoretic mobility (μ_{ep}; negative sign indicates flow in the direction of the anode, eq 3) and the EOF (μ_{EOF}). The apparent mobility can be calculated from the nanoslit length, L, the applied external electric field, V, and the migration time, t (see eq 3).

$$\mu_{app} = \mu_{EOF} + (-\mu_{ep}) = \frac{L^2}{Vt} \quad (3)$$

Figure 3 shows μ_{app} of AgNPs under different electrokinetic operating conditions (additional histograms are available in the Supporting Information; see Figure S4). The μ_{app} values observed were in the range of 2.0×10^{-5} to 9.0×10^{-5} cm^2/(Vs). For the high ionic strength carrier electrolyte, the apparent mobility of the AgNPs was higher compared to the use of a lower ionic strength buffer for both AgNP sizes. In addition, we noticed that as the nanocolumn depth approached the particle diameter, a reduction in the electrophoretic mobility of the AgNPs was observed (Figure 3B).

The electrophoretic velocity of a particle can be calculated using

$$\nu_{ep} = -f_H(\kappa, r)\frac{2\varepsilon_0\varepsilon_r\zeta_p}{3\eta}E \quad (4)$$

where ζ_p is the zeta potential of the particle and f_H is Henry's function (Smoluchowski approximation), which depends on r (radius) of the particle and its λ_D and represents the retardation effect of particles in electrophoresis.[50,51] In systems with a thick λ_D, the effective electric field within the EDL cannot be considered uniform and depends on ζ_p and the ratio of r and λ_D.[17,52]

When AgNPs are in an ionic buffer such as citrate, the surface is covered with citrate ions acting as a capping agent to prevent agglomeration of the AgNPs. The surface groups induce a charge on the particle, which is represented by ζ_p. At 0.05 mM citrate buffer concentrations, ζ_p of the 60 nm AgNPs was approximately –43 mV and for the 100 nm AgNPs, it was –46 mV (see Table S1). ζ_p plays a role in determining the particle's electrophoretic mobility as noted by eq 4.[17] On the basis of the direction of the EOF in the O$_2$ plasma treated PMMA devices and the observed apparent mobilities, we would expect the 60 nm particles to possess a smaller electrophoretic mobility compared to the 100 nm particles (see eq 3). However, on the basis of eq 4 and dividing ν_{ep} by E, which represents the particle's electrophoretic mobility, we would expect the 60 nm particles to have a larger apparent mobility compared to the 100 nm particles based solely on differences in ζ_p. The effects of viscous retardation, which is given by f_H, Henry's function, must be considered as well in terms of the electrophoretic mobility. For the 60 nm particles, f_H should be smaller than that for the 100 nm AgNPs.[17] As a note, because the EOF runs in the opposite direction of the electrophoretic mobility of the AgNPs due to the negative charge on the polymer walls following O$_2$ plasma treatment[34] and the negative charges carried by the citrate capped AgNPs, the apparent mobility will show lower values when the electrophoretic mobility of the AgNP is higher.

Napoli et al.[17] reported that 100 nm polystyrene beads possessed a higher apparent mobility than 50 nm beads in 1 mM buffer and 250 nm deep nanoslits. There were two effects that governed the particle velocity; viscous retardation near a nonconducting boundary, which is described by f_H, and the electric field effects on the particle.[17,53,54] By tuning the concentration of the buffer, which had an effect on the particles' and channel walls' EDL, it was possible to separate nanoparticles based on differences in their size.[55] Liu and co-workers were unable to separate AgNPs based on their size (17 nm AgNPs versus 49 nm AgNPs; % size difference = 49%; % size difference = (size difference)/(average particle size)) using conventional CE; the separation was successful only upon addition of SDS to the running electrolyte.[37] However, we were able to separate the 60 and 100 nm AgNPs (% size difference = 50%) using free solution electrophoresis and the polymer nanoslits (see Figure 2).

Determining Nanoslit Diffusion Coefficients

The effective diffusion coefficient (D_{eff}) defines the spatial distribution function of a particle with time. For a particle that undergoes Brownian motion only, the Stokes–Einstein relation[56] can be used to calculate the molecular diffusion coefficient, D_T

$$D_T = \frac{k_B T}{\gamma} \quad (5)$$

where k_B is Boltzmann's constant, T is the absolute temperature of the solution, and γ is the hydrodynamic Stokes drag coefficient of the particle, which is given by $\gamma = 6\pi\eta r$ where r is the particle radius and η is the solution viscosity. D_T values for the 60 nm AgNPs ranged from 7.27×10^{-12} to 9.04×10^{-12} m^2/s and for the 100 nm AgNPs it was 4.30×10^{-12} to 5.33×10^{-12} m^2/s (particle diameter distribution provides the range for D values, see Table S1).

Experimentally, the diffusion coefficient can be determined from the electrophoretic peak variance (σ^2) when the peak is fit to a Gaussian function and the major contribution to the zone variance is restricted to longitudinal diffusion. The effective diffusion coefficient (D_{eff}) under these conditions is given by

$$D_{eff} = \frac{\sigma^2}{2t} \quad (6)$$

While D_{eff} should be comparable to D_T when D_{eff} is calculated using eq 6, other dispersion factors can come into play such as Taylor dispersion, wall–particle interactions, Joule heating (which is minimal in our case), or other band broadening factors that would make D_{eff} differ from D_T.[57] D_{eff} can also depend on other factors as well, such as ζ, λ_D, and r.[52,58] We sought to evaluate D_{eff} for the 60 and 100 nm AgNPs using nanoscale electrophoresis.

Time histograms for single AgNPs electrokinetically moving through the PMMA nanoslits could be fit to a Gaussian function (see Figure 2) to determine the total zone variance (σ^2) from which D_{eff} could be deduced.

The time a single particle takes to travel through a nanoslit is given by eq 3 and the variance of particle travel times is given by eq 6. Combining eqs 3 and 6, the following relationship could be derived

$$\sigma^2 = \left(\frac{2D_{eff}L^2}{\mu_{app}} \right) \left(\frac{1}{V} \right) \quad (7)$$

For each applied voltage (V), the standard deviation (σ), which is the square root of the variance, could be extracted from the width of a Gaussian electrophoretic peak at the point of inflection. $\sigma(t)$ values obtained as such were converted to $\sigma(l)$ by multiplying each σ value with the average velocity at a particular voltage.

Using eq 6, D_{eff} of the AgNPs at different experimental conditions were calculated. Table 1 shows the values for D_{eff} at electric field strengths where minimal stick/slip motion was observed (500 and 1500 V/cm). D_{eff} and D_T were compared using , which was defined as follows

$$\Delta = \frac{D_{\text{eff}}}{D_{\text{T}}} \quad (8)$$

When the zonal variance is dominated by longitudinal diffusion, will approach 1.[57] As can be seen in Table 1, values in all cases studied were >10 irrespective of the concentration of the carrier electrolyte and the depth of the nanoslit. Because $D_{\text{eff}} > D_{\text{T}}$, longitudinal dispersion was not the only mechanism giving rise to the zone variance. We suspect that the distribution in the particle size (see Table S1), which causes variances in the particles' ζ, f_{H}, λ_{D}, and r values, was another major contributor to zonal variance.[52,58]

We observed transverse diffusion (see Figure S3) during migration through the nanoslit. On the basis of D_{eff} values for the 60 and 100 nm particles, they can travel ~0.5 μm and ~0.4 μm per frame, respectively, based on Brownian motion (for the 100 V/cm field strength and 48 frames during the total column transit, this amounts to a total Brownian motion distance of 19 and 24 μm for the 100 and 60 nm AgNPs). Because the nanoslit is 5 μm wide and approximately 100 μm in length, the nanoparticles can freely diffuse in the transverse (y-coordinate) and longitudinal (x-coordinate) directions. However, their diffusion is restricted in the z-direction due to the nanoscale dimension (150 and 400 nm depth of nanoslit) and electrostatic interactions with the walls.

Separation Efficiency and Resolution of Nanoscale Electrophoresis

Nanoscale electrophoresis can be evaluated in terms of the theoretical plates, N, given by

$$N = \frac{\mu_{\text{avgapp}}V}{2D_{\text{T}}} = \frac{L^2}{2D_{\text{T}}t_{\text{avg}}} \quad (9)$$

In Table 2, N is presented as a function of different nano-CE operating conditions. It was noted that N increased with increasing electric field strength over the range of field strengths investigated (Figure S5); at 1500 V/cm, N increased 10-fold compared to that observed at 100 V/cm for all nanoslits and buffer conditions investigated (see Figure S5 and Table 2). We could not test higher electric field strengths due to the limited frame rate we could achieve with our CCD.

In our experiment, we evaluated N at field strengths up to 1500 V/cm for columns that were 100 μm in length. In conventional CE, Joule heating limits the electric field strength that can be used. However, because of the high surface-to-volume ratio of the nanoslits, thermal effects did not seem to affect N at these high field strengths compared to larger sized columns, for example, microchannels (see Figure S5).[59] Hence, potentially higher field strengths can be used for nanoscale columns without observing deleterious effects in N.

When two species electrophorese in a column with average migration times, t_{R1} and t_{R2}, the resolution of the separation is given by

$$R_S = \frac{2(t_{R1} - t_{R2})}{1.7(W_{0.5,1} + W_{0.5,2})} \quad (10)$$

where $W_{0.5,1}$ and $W_{0.5,2}$ correspond to the width of the two peaks at half-maximum of the Gaussian peaks obtained from the histograms shown in Figure 2. The calculated resolution values are presented in Table 2. The optimal R_S (1.1) was achieved in 150 nm nanoslits using 0.05 mM citrate and an electric field strength of 1500 V/cm. We noted a decrease in resolution at lower electric field strengths most likely due to a combination of longitudinal diffusion and stick/slip motion occurring at the lower electric fields.

In the absence of stick/slip motion ($E > 200$ V/cm), we would expect to see better electrophoretic resolution for these nanoparticles when $d/\lambda_D < 10$ and the charge on the nanoslit walls is the same as that of the AgNPs. Inspection of the data in Table 2 indicated that the 150 nm deep nanoslits produced better resolution when using a 0.05 mM citrate buffer compared to the higher concentration citrate buffer. In addition, the 150 nm deep nanoslits produced better electrophoretic resolution compared to the 400 nm deep nanoslits (see Table 2 for the 500 and 1500 V/cm separations). At low electric field strengths ($E < 200$ V/cm), stick/slip motion affects the resulting resolution for the 150 nm nanoslits. We did not observe stick/slip motion of the AgNPs at all electric field strengths investigated for the 400 nm deep nanoslits.

The high-resolution values seen for the 150 nm deep nanoslits at 0.05 mM citrate buffer also resulted from the effects of transverse electromigration, TEM.[15,17,19] Because of electrostatic considerations arising from the similar charge on the walls of the nanoslits and the AgNPs, the particles are placed in different streamlines based upon their zeta potentials (see Table S1) when traveling through the nanoslits and confines their travel to those streamlines.[15] For plug flow, the resulting velocities would be unaffected by the transverse position of the particle. However, in cases where $d/\lambda_D < 10$, parabolic flow develops and, thus, can impart differences in the electrophoretic mobilities of the particles improving the resolution as noted in our results (see Table 2), especially for the lower citrate buffer concentrations where the EDL would show more overlap. In addition, at the lower citrate buffer concentration, ζ of the two nanoparticles were different as well (see Table S1).

On the basis of the supposition that the ζ was higher for the 100 nm particles, especially at the lower citrate concentration (see Table S1), and due to the like charges of both particle sizes and the nanoslit walls, the 100 nm particles would be expected to have a higher electrophoretic mobility compared to the 60 nm AgNP because electrostatic considerations would place them closer to the channel center line where the velocity would be higher for parabolic flow. Indeed, this was the case upon inspection of the data shown in Figure 3. While the apparent mobility of the 100 nm AgNPs was smaller compared to the 60 nm particles, this would imply a larger electrophoretic mobility for the 100 nm particles due to EOF considerations (see eq 3).

It has been reported that a decrease in R_S results when transitioning from micro- to nanoscale electrophoresis for batch type CE experiments that are accompanied by multiple particle occupancy within the nanoslit.[17,18] For example, Napoli and Pennathur noticed a decrease in plate numbers resulting in lower R_S for polystyrene beads in glass nanoslits. They suggested that the negatively charged particles and negatively charged channel walls played a significant role in affecting R_S.[17] Also, electrostatic repulsion of the polystyrene beads from the channel walls pushed the nanoparticles to the center of the channel, which increased the local concentration of the beads within the center of the channel leading to changes in viscous retardation. In our case, the probability of finding more than one particle in the nanoslit was below 0.01% (see eq 1). Therefore, we did not expect to see changes in the viscous retardation due to electrostatic effects.

EOFs are typically higher in nonmodified glass electrophoresis devices compared to PMMA devices that have been activated with an O_2 plasma.[34] The surface charge characteristics and the effects of pH on the EOF of polymer devices has been discussed in detail in a recent publication by our group.[34] For PMMA nanoslits, the surface charge was found to be −38.3 mC/m^2 with a ζ value of −57.1 mV. The measured EOF in the nanoslits was $0.93 \pm 0.02 \times 10^{-4}$ $cm^2/(V\ s)$. This value was lower than that reported for fused silica.[60] Considering that the migration time of a given particle is affected by the EOF and μ_{ep}, a negatively charged particle will spend more time in a channel under high EOF conditions giving rise to lower plate numbers and therefore reduced resolution. Compared to untreated glass devices, we expect polymer-based nanofluidic devices to provide improved resolution for negatively charged entities in nanoscale electrophoretic separations due to the associated lower EOF. Also, because of lower surface charge and the ability to control the surface charge by controlled dosing of the channel walls with the O_2 plasma, polymer nanoslits and nanochannels obviate the deleterious effects of concentration polarization.

CONCLUSIONS

AgNPs were used as a model system to investigate the utility of nanoscale electrophoresis using thermoplastic columns activated using O_2 plasma generating negatively charged surface functional groups (carboxylic acids) to support an EOF. Free solution mobility differences for 60 and 100 nm AgNPs were observed using PMMA nanoslits ~100 μm in length that were not seen using a microchannel column.[37] The electrophoresis separation differences in terms of resolution using free solution electrophoresis between the polymer nanoslits and the glass capillary arose from EDL overlap and electrostatic effects exerted on the migrating AgNP. Partial overlap of the EDL generated nonplug like flow at low buffer concentrations and coupled with TEM and larger differences in ζ of the 60 and 100 nm AgNPs at the lower carrier electrolyte concentration (see Table S1), provided separations in free solution that were not observed for glass microscale capillaries. In addition, the low EOF values associated with the thermoplastic columns provided improved resolution using free solution electrophoresis.

The separation of the AgNPs using PMMA-based nanoslit columns was demonstrated with a 50-fold improvement in N using $E = 1500$ V/cm compared to 100 V/cm and $R_S > 1$ in less than 2 s. Further improvements in the electrokinetic separation could be realized by using

higher electric field strengths and smaller sized column cross-sectional areas to further reduce deleterious effects produced by stick/slip motion and/or longitudinal diffusion.

In this work, thermoplastic columns were used, which provided several advantages compared to glass-based nanocolumns. For example, reduced surface charge mitigated issues with concentration polarization. In addition, the nanocolumns could be produced at low-cost and in high production modes using imprinting.

Supplementary Material

Refer to Web version on PubMed Central for supplementary material.

Acknowledgments

References

1. Dolník V, Liu S, Jovanovich S. Electrophoresis. 2000; 21:41–54. [PubMed: 10634469]

2. Pumera M, Wang J, Grushka E, Polsky R. Anal Chem. 2001; 73:5625–5628. [PubMed: 11816598]

3. Kinsella, A., Minteer, S. Molecular Biomethods Handbook. Walker, J., Rapley, R., editors. Humana Press; Totowa, NJ: 2008. p. 851-859.

4. Nilsson C, Birnbaum S, Nilsson S. J Chromatogr A. 2007; 1168:212–224. [PubMed: 17719051]

5. Osiri JK, Shadpour H, Park S, Snowden BC, Chen Z-Y, Soper SA. Electrophoresis. 2008; 29:4984–4992. [PubMed: 19130578]

6. Osiri J, Shadpour H, Soper S. Anal Bioanal Chem. 2010; 398:489–498. [PubMed: 20614109]

7. Lin C-H, Lee G-B, Chen S-H, Chang G-L. Sens Actuators, A. 2003; 107:125–131.

8. Turner SW, Cabodi M, Craighead HG. Phys Rev Lett. 2002; 88:128103. [PubMed: 11909505]

9. Danelon C, Santschi C, Brugger J, Vogel H. Langmuir. 2006; 22:10711–10715. [PubMed: 17129050]

10. Han J, Craighead HG. Science. 2000; 288:1026–1029. [PubMed: 10807568]

11. Woods LA, Gandhi PU, Ewing AG. Anal Chem. 2005; 77:1819–1823. [PubMed: 15762591]

12. Bayley H, Martin CR. Chem Rev. 2000; 100:2575–2594. [PubMed: 11749296]

13. Kemery PJ, Steehler JK, Bohn PW. Langmuir. 1998; 14:2884–2889.

14. Kuo T-C, Sloan LA, Sweedler JV, Bohn PW. Langmuir. 2001; 17:6298–6303.

15. Pennathur S, Santiago JG. Anal Chem. 2005; 77:6782–6789. [PubMed: 16255574]

16. Pennathur S, Santiago JG. Anal Chem. 2005; 77:6772–6781. [PubMed: 16255573]

17. Napoli M, Atzberger P, Pennathur S. Microfluid Nanofluid. 2011; 10:69–80.

18. Wynne T, Dixon A, Pennathur S. Microfluid Nanofluid. 2012; 12:411–421.

19. Baldessari F, Santiago J. J Nanobiotechnol. 2006; 4:12.

20. Yuan Z, Garcia AL, Lopez GP, Petsev DN. Electrophoresis. 2007; 28:595–610. [PubMed: 17304495]

21. Pennathur S, Santiago JG. Anal Chem. 2005; 77:6772–6781. [PubMed: 16255573]

22. Xuan X, Li D. Electrophoresis. 2006; 27:5020–5031. [PubMed: 17124708]

23. Xuan X. Electrophoresis. 2008; 29:3737–3743. [PubMed: 18850643]

24. Garcia AL, Ista LK, Petsev DN, O'Brien MJ, Bisong P, Mammoli AA, Brueck SRJ, Lopez GP. Lab Chip. 2005; 5:1271–1276. [PubMed: 16234951]

25. Cheng L-J, Guo LJ. ACS Nano. 2009; 3:575–584. [PubMed: 19220010]

26. Austin MD, Ge HX, Wu W, Li MT, Yu ZN, Wasserman D, Lyon SA, Chou SY. Appl Phys Lett. 2004; 84:5299–5301.

27. Chou SY, Krauss PR. Microelectron Eng. 1997; 35:237–240.

28. Chou SY, Krauss PR, Renstrom PJ. Appl Phys Lett. 1995; 67:3114–3116.

29. Chou SY, Krauss PR, Renstrom PJ. J Vac Sci Technol B: Microelectron Process Phenom. 1996; 14:4129–4133.

30. Gates BD, Whitesides GM. J Am Chem Soc. 2003; 125:14986–14987. [PubMed: 14653723]

31. Abgrall P, Low L-N, Nguyen NT. Lab Chip. 2007; 7:520–522. [PubMed: 17389971]

32. Chantiwas R, Hupert ML, Pullagurla SR, Balamurugan S, Tamarit-Lopez J, Park S, Datta P, Goettert J, Cho YK, Soper SA. Lab Chip. 2010; 10:3255–3264. [PubMed: 20938506]

33. Thamdrup LH, Klukowska A, Kristensen A. Nanotechnology. 2008; 19:125301. [PubMed: 21817722]

34. Uba FI, Pullagurla SR, Sirasunthorn N, Wu J, Park S, Chantiwas R, Cho Y-K, Shin H, Soper SA. Analyst. 2015; 140:113–126. [PubMed: 25369728]

35. Uba FI, Hu B, Weerakoon-Ratnayake K, Oliver-Calixte N, Soper SA. Lab Chip. 2015; 15:1038–1049. [PubMed: 25511610]

36. Radko SP, Chrambach A. J Chromatogr Biomed Appl. 1999; 722:1–10.

37. Liu F-K, Ko F-H, Huang P-W, Wu C-H, Chu T-C. J Chromatogr A. 2005; 1062:139–145. [PubMed: 15679152]

38. Harms ZD, Selzer L, Zlotnick A, Jacobson SC. ACS Nano. 2015; 9:9087–9096. [PubMed: 26266555]

39. Wu JH, Chantiwas R, Amirsadeghi A, Soper SA, Park S. Lab Chip. 2011; 11:2984–2989. [PubMed: 21779601]

40. Huang T, Nallathamby PD, Xu X-HN. J Am Chem Soc. 2008; 130:17095–17105. [PubMed: 19053435]

41. Nallathamby PD, Lee KJ, Xu XHN. ACS Nano. 2008; 2:1371–1380. [PubMed: 19206304]

42. Lee KJ, Nallathamby PD, Browning LM, Osgood CJ, Xu XHN. ACS Nano. 2007; 1:133–143. [PubMed: 19122772]

43. Goldberg RN, Kishore N, Lennen RM. J Phys Chem Ref Data. 2002; 31:231–370.

44. Plecis A, Schoch RB, Renaud P. Nano Lett. 2005; 5:1147–1155. [PubMed: 15943459]

45. Chantiwas R, Hupert ML, Pullagurla SR, Balamurugan S, Tamarit-Lopez J, Park S, Datta P, Goettert J, Cho Y-K, Soper SA. Lab Chip. 2010; 10:3255–3264. [PubMed: 20938506]

46. Campbell LC, Wilkinson MJ, Manz A, Camilleri P, Humphreys CJ. Lab Chip. 2004; 4:225–229. [PubMed: 15159783]

47. Luan B, Afzali A, Harrer S, Peng H, Waggoner P, Polonsky S, Stolovitzky G, Martyna G. J Phys Chem B. 2010; 114:17172–17176. [PubMed: 21128651]

48. Novak BR, Moldovan D, Nikitopoulos DE, Soper SA. J Phys Chem B. 2013; 117:3271–3279. [PubMed: 23461845]

49. Xia K, Novak BR, Weerakoon-Ratnayake KM, Soper SA, Nikitopoulos DE, Moldovan D. J Phys Chem B. 2015; 119:11443. [PubMed: 26237155]

50. Ohshima H. J Colloid Interface Sci. 2002; 252:119–125. [PubMed: 16290770]

51. Hunter, RJ. Zeta Potential in Colloid Science: Principles and Applications. Vol. 2. Academic Press; London: 2013.

52. Henry DC. Proc R Soc London, Ser A. 1931; 133:106–129.

53. Xuan X, Xu B, Li D. Anal Chem. 2005; 77:4323–4328. [PubMed: 16013842]

54. Xuan X, Raghibizadeh S, Li D. J Colloid Interface Sci. 2006; 296:743–748. [PubMed: 16226268]

55. Schnabel U, Fischer C-H, Kenndler E. J Microcolumn Sep. 1997; 9:529–534.

56. Einstein A. Ann Phys. 1905; 322:549–560.

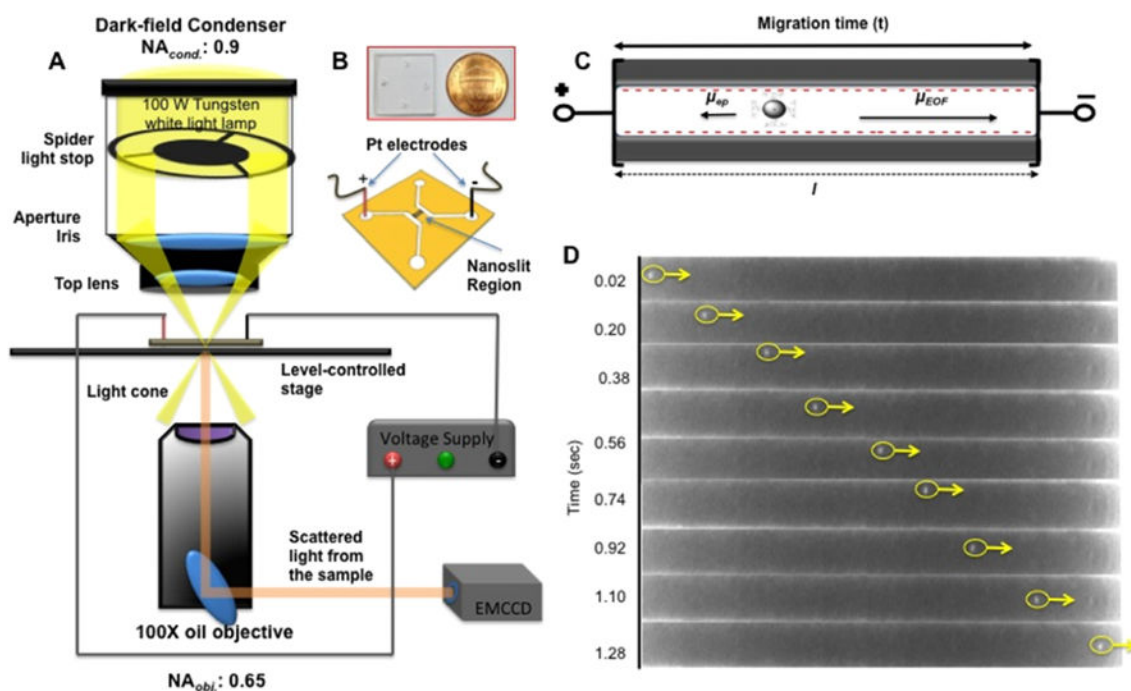57. Batz NG, Mellors JS, Alarie JP, Ramsey JM. Anal Chem. 2014; 86:3493–3500. [PubMed: 24655020]

58. Kirby BJ, Hasselbrink EF. Electrophoresis. 2004; 25:187–202. [PubMed: 14743473]

59. Jorgenson JW, Lukacs KD. Science. 1983; 222:266–272. [PubMed: 6623076]

60. Menard LD, Mair CE, Woodson ME, Alarie JP, Ramsey JM. ACS Nano. 2012; 6:9087–9094. [PubMed: 22950784]
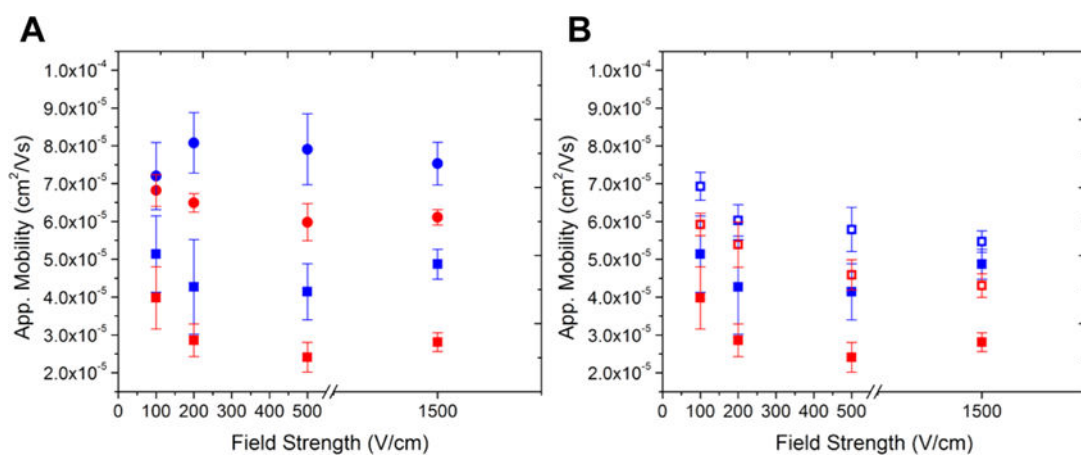
Figure 1.
(A) Schematic of the dark-field microscope and the experimental setup. The sample was mounted on a level-controlled microscope stage. While the spider stop controlled white light missed the objective, only scattered light from the sample entered the objective. (B) Image of the PMMA nanofluidic chip and a schematic of the device with nanoslits. (C) Schematic of the nanoslits when an external electric field was applied. Electroosmotic flow was from anode to cathode while the electrophoretic mobility of negatively charged AgNPs was toward the anode. (D) Representation of a translocation event for a 60 nm AgNP in a nanoslit. Time-lapse image sequence of the single AgNP event at an external field strength of 200 V/cm. The particle translocation direction was from anode to cathode (same direction as EOF) with a translocation time for this event of 1.3 s. Dimensions of the nanoslits were 100 μm in length, 5 μm wide and 150 nm deep.
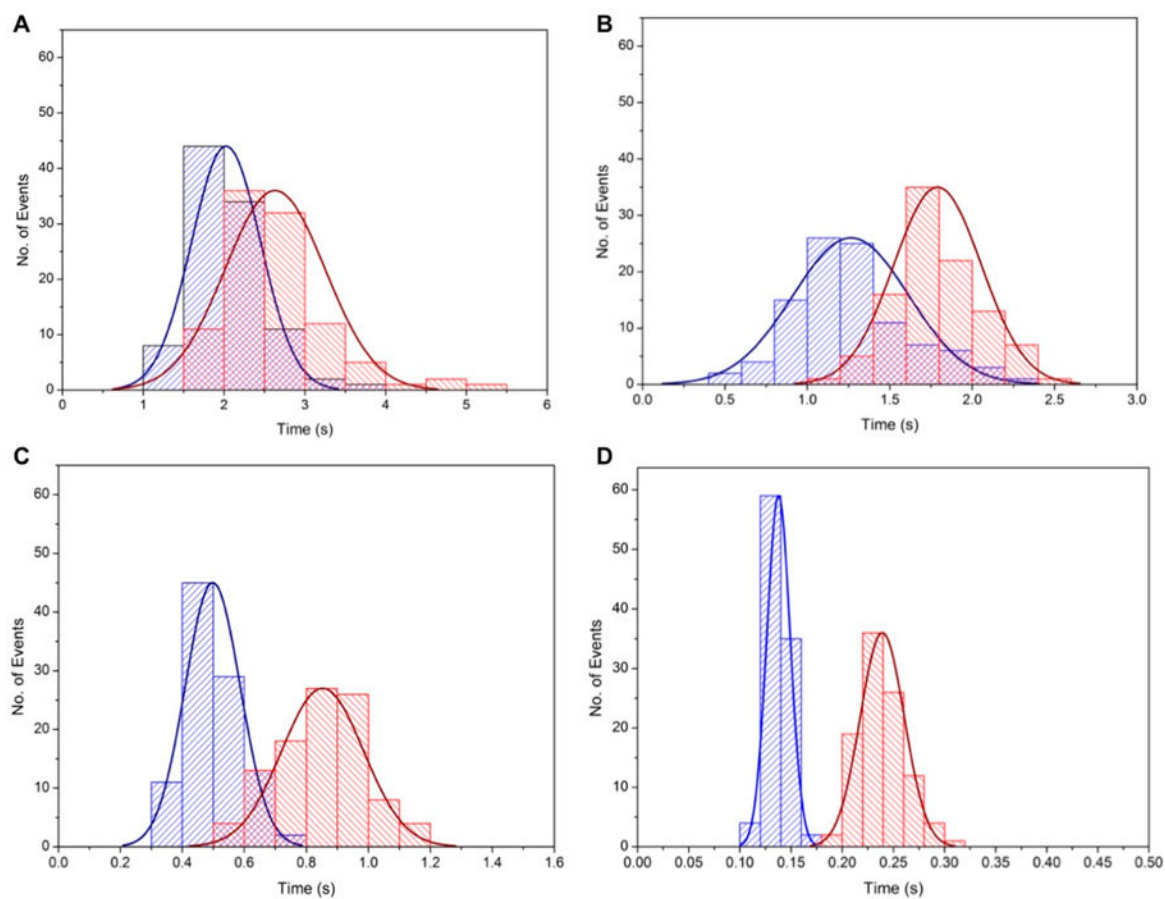
Figure 2.
Histograms of translocation events for 60 nm AgNPs (blue) and 100 nm AgNPs (red) in 150 nm nanoslits with a running buffer of 0.05 mM citrate. Each histogram includes 100 events at a bias voltage of (A) 100 V/cm, (B) 200 V/cm, (C) 500 V/cm, and (D) 1500 V/cm. Note that the time axes have different scales depending on the electric field.

Figure 3.
Apparent mobility of AgNPs in PMMA nanoslits. Data points corresponding to 60 nm AgNPs are represented in blue while 100 nm AgNPs are represented in red. Each data point represents the mean of 100 translocation events with the error bars depicting the standard deviation. Closed squares correspond to the electrophoresis data in 0.05 mM citrate buffer and 150 nm deep nanoslits. Closed circles represent data for 150 nm nanoslits with a running buffer of 2.0 mM citrate. Open squares represent data for the 400 nm deep nanoslits in 0.05 mM citrate buffer. (A) Comparison of the apparent mobilities in citrate buffer concentrations of 0.05 mM and 2.0 mM. (B) Comparison of the apparent mobilities as a function of nanoslit depth, 150 nm versus 400 nm.

Table 1

Calculated Effective Diffusion coefficient and the Ration of Effective Diffusion coefficient to Molecular Diffusion coefficient Given by at High Voltages for All the Experimental Conditions[a]

Depth of Nanoslit	150 nm		150 nm		150 nm	
Citrate Buffer Concentration	2.00 mM		0.05 mM		0.05 mM	
Particle Size (nm)					150 nm	
Field Strength (V/cm)	60	100	60	100	60	100
Effective Diffusion Coefficient, D_{eff} ($\times 10^{-10}$, m²/s)						
500	2.79	1.06	3.20	1.40	1.33	0.955
1500	3.33	0.513	2.46	1.70	1.15	1.81
Field Strength (V/cm)	$= D_{eff}/D_T$					
500	34.2	22.1	39.2	29.2	16.3	19.8
1500	40.9	10.6	30.1	35.2	14.1	37.7

[a] The diffusion coefficients are given in m²/s.

Table 2

Electrophoretic Parameters for 60 and 100 nm AgNPs at Different Nanoscale Electrophoresis Operating Conditions

Depth of Nanoslit	150 nm		150 nm		400 nm	
Citrate Buffer Concentration	**2.00 mM**		**0.05 mM**		**0.05 mM**	
Particle Size (nm)	**60**	**100**	**60**	**100**	**60**	**100**
Field Strength (V/cm)	**Plate Number (N)**					
100	723	694	303	233	422	371
200	987	1,320	486	570	737	1,090
500	2,350	3,000	1,220	1,200	1,750	2,320
1500	6,800	9,270	4,370	4,250	5,100	6,370
Field Strength (V/cm)	**Resolution (R)**					
100	0.089		0.022		0.58	
200	0.77		0.33		0.26	
500	0.57		0.74		0.51	
1500	0.67		1.1		0.61	